

# 1 Snow accumulation and ablation measurements in a mid-latitude 2 mountain coniferous forest (Col de Porte, France, 1325 m alt.): The 3 Snow Under Forest (SnoUF) field campaigns dataset

4 Jean Emmanuel Sicart<sup>1</sup>, Victor Ramseyer<sup>1</sup>, Ghislain Picard<sup>1</sup>, Laurent Arnaud<sup>1</sup>, Catherine Coulaud<sup>1</sup>,  
5 Guilhem Freche<sup>1</sup>, Damien Soubeyrand<sup>1</sup>, Yves Lejeune<sup>2</sup>, Marie Dumont<sup>2</sup>, Isabelle Gouttevin<sup>2</sup>, Erwan Le  
6 Gac<sup>2</sup>, Frederic Berger<sup>3</sup>, Jean-Matthieu Monnet<sup>3</sup>, Laurent Borgniet<sup>3</sup>, Eric Mermin<sup>3</sup>, Nick Rutter<sup>4</sup>, Clare  
7 Webster<sup>5,6</sup>, Richard Essery<sup>7</sup>.

8 <sup>1</sup> Univ. Grenoble Alpes, IRD, CNRS, Grenoble INP, IGE, 38000 Grenoble, France.

9 <sup>2</sup> CNRM UMR 3589, Météo-France/CNRS, Centre d'Études de la Neige, Grenoble, France

10 <sup>3</sup> Univ. Grenoble Alpes, INRAE, LESSEM, 2 rue de la Papeterie-BP 76, St-Martin-d'Hères, F-38402, France.

11 <sup>4</sup> Department of Geography and Environmental Sciences, Northumbria University, Newcastle upon Tyne, NE1 8ST, UK

12 <sup>5</sup> WSL Swiss Federal Institute for Snow and Avalanche Research SLF, Davos, Switzerland

13 <sup>6</sup> Department of Geosciences, University of Oslo, Norway

14 <sup>7</sup> School of GeoSciences, University of Edinburgh, UK

15 *Correspondence to:* Jean Emmanuel Sicart (jean-emmanuel.sicart@ird.fr)

16 **Abstract.** Forests strongly modify the accumulation, metamorphism and melting of snow in mid and high-latitude regions.  
17 Recently, snow routines in hydrological and land surface models have been improved to incorporate more accurate  
18 representations of forest snow processes, but model inter-comparison projects have identified deficiencies, partly due to  
19 incomplete knowledge of the processes controlling snow cover in forests. The Snow Under Forest (SnoUF) project was  
20 initiated to enhance knowledge of the complex interactions between snow and vegetation. Two field campaigns, during the  
21 winters 2016-17 and 2017-18, were conducted in a coniferous forest bordering the snow study at Col de Porte (1325 m a.s.l,  
22 French Alps) to document the snow accumulation and ablation processes. **This paper presents the field site, instrumentation,  
23 and collection and post-processing methods.** The observations include distributed forest characteristics (tree inventory, LIDAR  
24 measurements of forest structure, sub-canopy hemispherical photographs), meteorology (**automatic weather station and an  
25 array of radiometers**), snow cover and depth (snow poles transect and laser scan), and snow interception by the canopy during  
26 precipitation events. The weather station installed under dense canopy during the first campaign has been maintained since  
27 then and provides continuous measurements throughout the year since 2018. Data are publicly available from the repository  
28 of the Observatoire des Sciences de l'Univers de Grenoble (OSUG) data center at <http://dx.doi.org/10.17178/SNOUF.2022>.

## 29 1 Introduction

30 Around 20% of Northern Hemisphere snow overlaps with forest (e.g., Rutter et al., 2009), and sub-canopy snow cover is  
31 closely related to eco-hydrological processes. Forests strongly modify the accumulation, metamorphism and melting of snow,  
32 they intercept part of the precipitation, modify radiation fluxes and surface roughness, and reduce albedo and wind speed (e.g.,  
33 Otterman et al., 1988; Pomeroy et al., 2008; Musselman et al., 2012; Essery, 2013). For example, the model inter-comparison  
34 project SnowMIP2 (Essery et al., 2009; Rutter et al., 2009) evaluated 33 forest snow models differing in both process  
35 complexity and canopy implementation approaches. Major deficiencies of modeling snow in forests were identified, and the  
36 project concluded that model performance was limited by incomplete knowledge of the processes controlling snow cover in  
37 forests. Since then, numerous measurement campaigns have been conducted (e.g., Webster et al. 2016, 2018; Malle, et al.,  
38 2019; Mazzotti et al., 2019; Hojatimalekshah et al., 2021) and snow routines in hydrological and land surface models have  
39 been enhanced to incorporate more accurate representations of forest snow processes (e.g., Ellis et al., 2013; Gouttevin et al.,  
40 2015; Boone et al., 2017; Mazzotti et al., 2020). However, these improved routines still represent canopy as one homogeneous  
41 layer without accounting for the effects of vertical canopy heterogeneity on snow accumulation and ablation processes.  
42 Detailed snow and meteorological measurements are therefore still required, and remain an important step to better understand  
43 the complex interactions between snow and vegetation. Col de Porte (CDP) is a mid-elevation site located at 1325 m altitude  
44 (45.295°N, 5.766°E) in the Chartreuse mountain range in France, with a meadow bordered by a coniferous forest. The CDP  
45 meadow site has been operated by CEN-MeteoFrance with daily measurements of snow depth, air temperature, and  
46 precipitation recorded since 1960 (Lejeune et al., 2019; Morin et al., 2012). Hourly measurements of meteorological and snow  
47 variables required to run and evaluate detailed snowpack models such as Crocus (Vionnet et al., 2012) started in 1987 and  
48 have been almost continuous during the snow seasons since 1993. CDP is part of several observation networks at the national  
49 scale (e.g., Observation pour l'Experimentation et la Recherche en Environnement CryObsClim and Systèmes d'Observation  
50 et d'Expérimentation au long terme pour la Recherche en Environnement des glaciers, GlacioClim) and at the international  
51 scale (e.g., ILTER European Research Infrastructure, WMO Global Cryosphere Watch CryoNet network, GEWEX INARCH).  
52 For more details, the reader is referred to Lejeune et al. (2019). Only a few studies have investigated the snow cover distribution  
53 in the forest of CDP (e.g., Durot, 1999); however, the immediate proximity of the forest parcel to the historical, long-term  
54 open-area snow observatory of CDP offers a good opportunity to understand and relate the sub-canopy meteorological and  
55 snow processes to their open-area counterparts.

56 Two field campaigns have been conducted in the conifer forest bordering the reference meadow site to document the snow  
57 accumulation and ablation processes: from 16 January 2016 to 21 March 2017 and from 1 December 2017 to 15 March 2018.  
58 This paper presents the measurement methods that were applied in the forest plot during these two field campaigns. The  
59 observations include distributed forest characteristics (tree inventory, LIDAR measurements of forest structure, sub-canopy  
60 hemispherical photographs), meteorological variables (automatic weather station and an array of radiometers), snow height  
61 and water equivalent (snow poles transect and laser scan), and transects of snow interception by the canopy during precipitation

62 events. The dataset also includes continuous measurements from the weather station in the forest from March 2018 to June  
63 2022. Complementing the datasets, the repository of the Observatoire des Sciences de l'Univers de Grenoble data center also  
64 includes technical information, photographs and a detailed plan of the instrumentation.

## 65 **2 Site and forest description**

### 66 **2.1 Site**

67 The study site is a triangular forest parcel of 2000 m<sup>2</sup> (Figure 1) next to the meadow where the historical open-area snow  
68 measurements are conducted. It is delimited by a fence along its south and northeast sides. Its west side corresponds to the  
69 edge between the forest and the open meadow area. The terrain slope is around 10° oriented toward east-north-east. The stand  
70 is dominated by Norway spruce (*Picea abies*) with young silver firs (*Abies alba*). Some broadleaved trees are located along  
71 the west edge. The parcel exhibits two gaps in the canopy. The smaller one is in the south-west, while the larger one is at the  
72 center and extends toward the south fence (Figure 2). During the first campaign, the annual maximum snow depth was around  
73 100 cm in the open site (meadow reference site) and only around 50 cm under the canopy. During the second campaign, the  
74 annual maximum snow depth was around 160 cm in the open site and 130 cm under the canopy.

75



76  
77  
78  
79  
80

Figure 1: Aerial photographs of the site taken on 30 August 2016, with locations of the sensors during the 2017-18 field campaign. On the left is the meadow with part of the long-term instrumentation for the Col de Porte site. Labels “2” and “3” refer to sensors SW2 and SW3.

81

## 2.2 Forest measurements

82

### 2.2.1 Manual forest inventory

83

An inventory of trees higher than 1.3 m took place during field campaigns between September 2016 and July 2018. On 13-14

84

September 2016, live and dead trees were inventoried, and the following observations and measurements were performed:

85

- diameter at breast height (DBH, measured with a tape measure at 1.3 m height above the ground, upslope of the tree);

86

- species;

87

- tree height measured with a Hagl f Vertex 4 hypsometer, only for trees with a DBH larger than 7.5 cm.

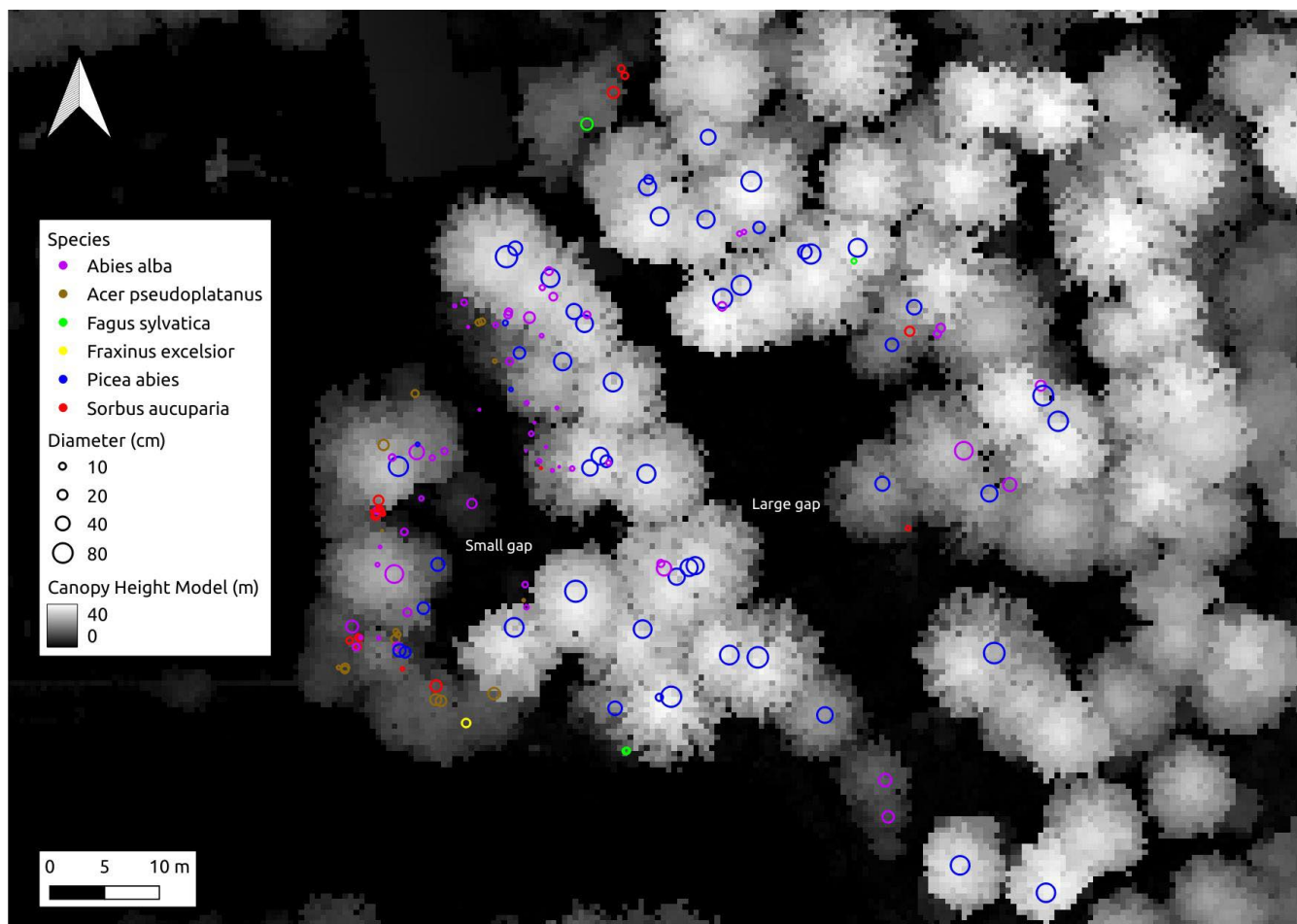
88 Tree identification numbers were painted on the trunk at a height around 1.3 m above ground. Three reference poles were  
 89 positioned in the site and geolocated using a Trimble GeoExplorer 6000 XH GNSS receiver. Trees were mapped relative to a  
 90 nearby pole by measuring the ground distance (Vertex 4 hypsometer), slope (clinometer) and azimuth (compass). Tree position  
 91 precision relative to the reference pole is expected to be better than 50 cm, whereas GNSS precision under the forest canopy  
 92 is of the order of a few meters. In total, 141 trees were inventoried, including 128 live trees, 3 dead trees and 10 stumps.  
 93 On 5 May 2017, vertical crown projections of live trees with a DBH larger than 7.5 cm were measured following the method  
 94 specified by Rohle (1986) but using a clinometer instead of a plummet to locate the crown extension. The horizontal distances  
 95 between the trunk center and the vertical projection of the furthest live branch along north, south, east and west directions were  
 96 measured with a tape. If several tree stems were sprouting from a common base, the whole clump was considered to have one  
 97 single crown and its extension was measured from the stem with the largest diameter in the clump. On 20 June 2017, tree  
 98 positions were measured with a Leica TS02 total station located in the open area at the west of the forest. The total station  
 99 position was recorded with a Trimble R2 differential GNSS receiver, ensuring centimetric accuracy. On July 25, 2018, heights  
 100 and crown extensions were measured on trees with a DBH smaller than 7.5 cm (Table 1). The tree inventory was extended  
 101 outside the southern fence to include trees which might cast shadows inside the forest parcel (DBH, height, crown extension,  
 102 species). Their positions were measured with slope (clinometer), azimuth (compass) and ground distance (Vertex 4  
 103 hypsometer) relative to a reference pole located with a GNSS receiver.

104  
 105 Table 1: Tree inventory on July 25, 2018

Species	Health status			
	Standing, live	Standing, dead	Cut between June 2017 and July 2018	Large stump (cut before Sept. 2016)
Abies alba	54	2	0	0
Picea abies	52	1	0	10
Sorbus aucuparia	20	0	1	0
Acer pseudoplatanus	15	0	1	0
Fagus sylvatica	4	0	0	0
Fraxinus excelsior	1	0	0	0

106  
 107 Tree easting and northing values in the RGF 93 - Lambert 93 projected coordinate system were then derived from the total  
 108 station coordinates if available, or from their polar coordinates relative to a reference pole. Tree altitude values were computed  
 109 from the airborne laser scanning data (see Section 2.2.2) by bilinear interpolation of the ground-classified points at the location  
 110 of trees. Figure 2 shows a map of inventoried live trees and canopy heights. In the forest stand inside the fence, most of the  
 111 trees are between 30 and 40 m high (Figure 3) and the total basal area is about 66.3 m<sup>2</sup>/ha. It includes 52 firs, 43 spruce and  
 112 33 broadleaved trees. Trees measured outside the southern fence included 9 spruce, 2 firs and 7 broadleaves. Tree position

113 accuracy is estimated to be better than 10 cm for the trees measured with the total station inside **the fenced area and around**  
114 50 cm for additional trees outside the fence. Luoma et al. (2017) reported a precision of 0.5 m (standard deviation) for height  
115 measurements with a Vertex 4 clinometer. Elzinga et al. (2005) reported a standard deviation of 0.5 cm for diameters measured  
116 with a tape measure. Measurement errors on crown extension is mostly due to the difficulty **of assessing** the vertical projection  
117 of the branches' extent on the ground. Accuracy is expected to be from 10 cm for small trees (height smaller than 4 m) to  
118 50 cm for the tallest ones (around 30 m).  
119



120  
121 Figure 2. **Map of inventoried live trees (2016-2018 campaigns) and canopy height model derived from airborne laser**  
122 **scanning acquired between 30 August and 2 September 2016.**  
123

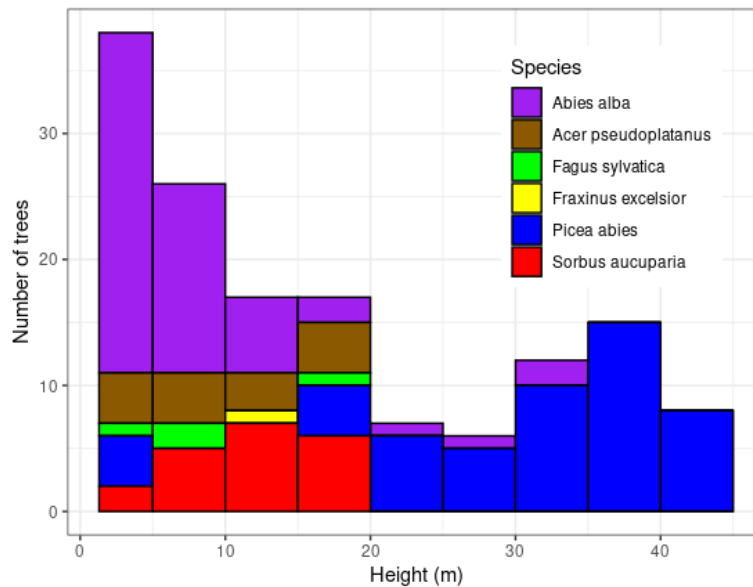


Figure 3: Height distribution of living trees taller than 1.3 m (2016-2018 campaigns).

### 2.2.2 Airborne remote sensing measurements

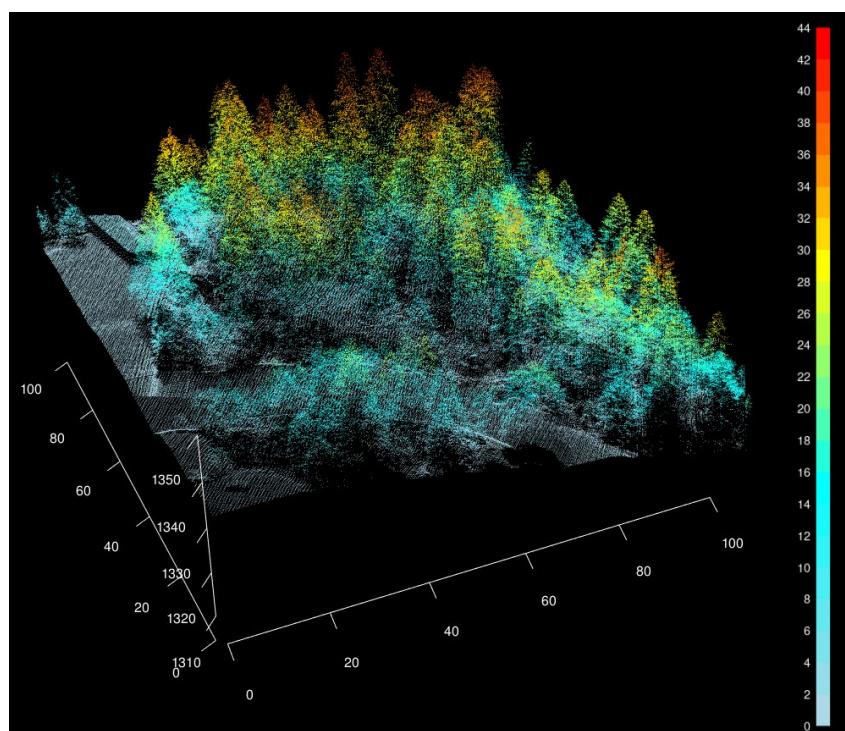
Airborne laser scanning (ALS) is a remote sensing technique based on LiDAR that can provide a 3D point cloud of forest structure. The point cloud can be processed to derive forest metrics used to parametrize snow interception, such as leaf area index or canopy closure (e.g., Helbig et al., 2020). ALS was acquired during a campaign covering 123.5 km<sup>2</sup> (which integrates the Col de Porte site) between 30 August and 2 September 2016, using a Riegl LMS Q680i sensor mounted on a helicopter. The scheduled flight height and speed were 750 m above ground and 70 knots, respectively. The scan frequency was 300 kHz with a scan angle of  $\pm 30^\circ$ . The aircraft trajectory was computed from the Inertial Measurement Unit and GPS data. Point coordinates were extracted and computed using the RiAnalyse and RiWorld software (<http://www.riegl.com/products/software-packages/>). The point cloud was then classified as ground/non-ground using Terrasolid (<https://terrasolid.com/>). To assess the accuracy of elevation measurements, 318 ground control points were measured with differential GNSS in 11 flat, vegetation-less plots. Differential GNSS horizontal accuracy is around 2-3 cm in such areas. Comparison of the control points with the point cloud yielded an altitudinal accuracy of 4.7 cm (root mean square error of differences), with a bias of -0.3 cm. The point cloud was delivered as tiled files in LAS format, which is the most common format for LiDAR point cloud exchange and is maintained by the ASPRS<sup>1</sup>. The coordinate system was RGF 93 - Lambert 93, with altitude in the system NGF-IGN69. The point cloud extracted on a 200 m radius disk centered on the study site was exported in a single compressed LAS file (v1.1

<sup>1</sup> <https://www.asprs.org/divisions-committees/lidar-division/laser-las-file-format-exchange-activities>

142 format 1). Pulse density in the study site is 17 points/m<sup>2</sup>, resulting in densities of 3.3 points/m<sup>2</sup> for ground points and 28  
143 points/m<sup>2</sup> with multiple returns for canopy points.

144 For the extent of the inventoried trees plus a 30 m buffer, digital surface models were computed at 0.5 m resolution from the  
145 ALS point cloud. The digital terrain model (DTM) was computed by estimating the altitude of each cell center by bilinear  
146 interpolation of ALS points classified as ground. The point cloud was normalized by subtracting the ground altitude at the  
147 position of each point, estimated by bilinear interpolation of ground points. A canopy height model (CHM) was computed by  
148 retaining the highest value of normalized heights in each cell. Cells without values were filled by the median of their 3×3  
149 neighborhood. The DTM and CHM were delivered as raster files in tif format. Aerial photographs were also taken during the  
150 ALS acquisition. Pictures were used to produce a 10 cm resolution RGB orthophoto provided as a tif file for the extent of the  
151 DTM. Figure 4 shows a perspective view of the 3D point cloud acquired by the airborne laser scanning.

152



153

154 Figure 4: Perspective view of the 3D point cloud of the area of interest acquired by airborne laser scanning between 30  
155 August and 2 September 2016. Points are colored according to their height above ground.

156

### 157 2.2.3 Hemispherical photographs

158 Hemispherical photographs were taken on 4 September 2017 at each radiometer location. Although the sky was not completely  
159 overcast, there was no direct sunlight. A Nikon Coolpix 4300 digital camera was used with a Nikon FC-E8 fisheye lens,  
160 mounted 60 cm above the ground surface on a tripod. The camera was aligned to north with a compass and carefully levelled



161 using a bubble level. All sites were snow-free when the hemispherical photographs were taken. Sky view factors were then  
162 calculated following Essery et al. (2008) assuming an equiangular lens projection. To distinguish vegetation from sky pixels,  
163 and to calculate the sky view factor at each location, a brightness threshold was selected manually for each hemispherical  
164 photograph (Figure 5). This allows us to account for variations in illumination conditions during changes in cloud cover or  
165 thickness. Brightness thresholds can be selected automatically (Nobis and Hunziker, 2005), but the manual process gave a  
166 clear distinction between canopy and sky pixels in every case here. Calculated sky view factors ranged from 0.15 to 0.35 at  
167 the radiometer sites, which were mostly situated under a rather dense canopy. Reid et al. (2014) estimated the uncertainty in  
168 the sky view factor using this method to be  $\pm 0.02$ .



170  
171 Figure 5: Example of a hemispherical photograph (left) and a binary image (right, white pixels are sky and black pixels are  
172 canopy, calculated sky view factor 0.25). The photograph was taken on 4 September 2017 at radiometer A1 (Figure 1).

### 173 3 Meteorological and snow observations in the forest

#### 174 3.1 Radiometer array

175 An array of 15 CMP3 Kipp & Zonen pyranometers and 11 CGR3 Kipp & Zonen pyrgeometers was deployed on the snow  
176 surface from dense canopy to an opening (Figure 1). During the first campaign, each radiometer was positioned horizontally  
177 with a bubble level on a wooden board placed on the snow surface. During the second campaign, the horizontal support of the  
178 radiometers was attached to a vertical bar fixed in the ground. The height of the support (10-20 cm) was adjusted to the snow  
179 surface every two or three days. This system allowed better stability and levelling of the radiometers. One-minute averages of  
180 the incoming radiation fluxes measured at five second time intervals were recorded by two Campbell Scientific CR3000 data  
181 loggers. Inter-calibration of the sensors before the campaigns led to estimates of sensor accuracies close to those announced  
182 by the manufacturer:  $\pm 12 \text{ W m}^{-2}$  for solar radiation and  $\pm 8 \text{ W m}^{-2}$  for longwave radiation, in accordance with uncertainty

183 estimations from similar sensors (Halldin and Lindroth 1992, Philipona et al. 2001, Michel et al. 2008, Van den Broeke et al.  
184 2004). The radiation data were carefully post-processed to remove periods when the sensors were snow covered or tilted.

### 185 3.2 Weather station

186 The weather station was installed under rather dense canopy (sky view factor  $\sim 0.2$ ) during the first campaign and has been  
187 maintained since then. Table 2 lists the sensors installed on the station, their specifications and their accuracy according to the  
188 manufacturers. The ultrasonic depth gauge measures the snow height. Ten temperature probes buried in the ground are used  
189 to estimate the heat conduction flux. 15-minute averages of the data measured at 10 second time intervals are recorded by a  
190 Campbell Scientific CR3000 data logger. An AXIS M1125-E camera took pictures of the surface around the weather station  
191 every three hours during daytime. These images were used to monitor surface and sensor conditions. A Campbell Scientific  
192 IR120 infrared sensor was used to measure the surface temperature of a trunk close to the meteorological station (Figure 1).  
193 One-minute averages of longwave irradiance measured at five second time intervals were recorded by a Campbell Scientific  
194 CR1000 data logger.

195  
196 Table 2: Variables measured by the weather station below the canopy along with the sensor type, heights and precision  
197 according to the manufacturers.

Quantity	Sensor Type	Height (cm) <sup>1</sup>	Accuracy according to the manufacturer
Air temperature, °C, and relative humidity, %	Campbell CS215C	210	$\pm 0.2^\circ\text{C}$ $\pm 2\%$ in [0-90%] $\pm 3\%$ in [90-100%]
Wind speed and direction, m s <sup>-1</sup> and degrees	Gill windsonic	210	$\pm 0.3 \text{ m s}^{-1}$ $\pm 3$ degrees
Incident and reflected short-wave radiation, W m <sup>-2</sup>	Kipp & Zonen CM3 0.3 < $\lambda$ < 2.8 $\mu\text{m}$	100	$\pm 10\%$ for daily sums
Incoming and outgoing long-wave radiation, W m <sup>-2</sup>	Kipp & Zonen CG3 5 < $\lambda$ < 50 $\mu\text{m}$	100	$\pm 10\%$ for daily sums
Surface elevation changes, mm	Ultrasonic depth gauge Campbell SR50	180	$\pm 1 \text{ cm}$
Temperature in the ground, °C	108 Campbell	-2.5, -8, -15, -30, -60 <sup>3</sup>	$\leq \pm 0.01^\circ\text{C}$

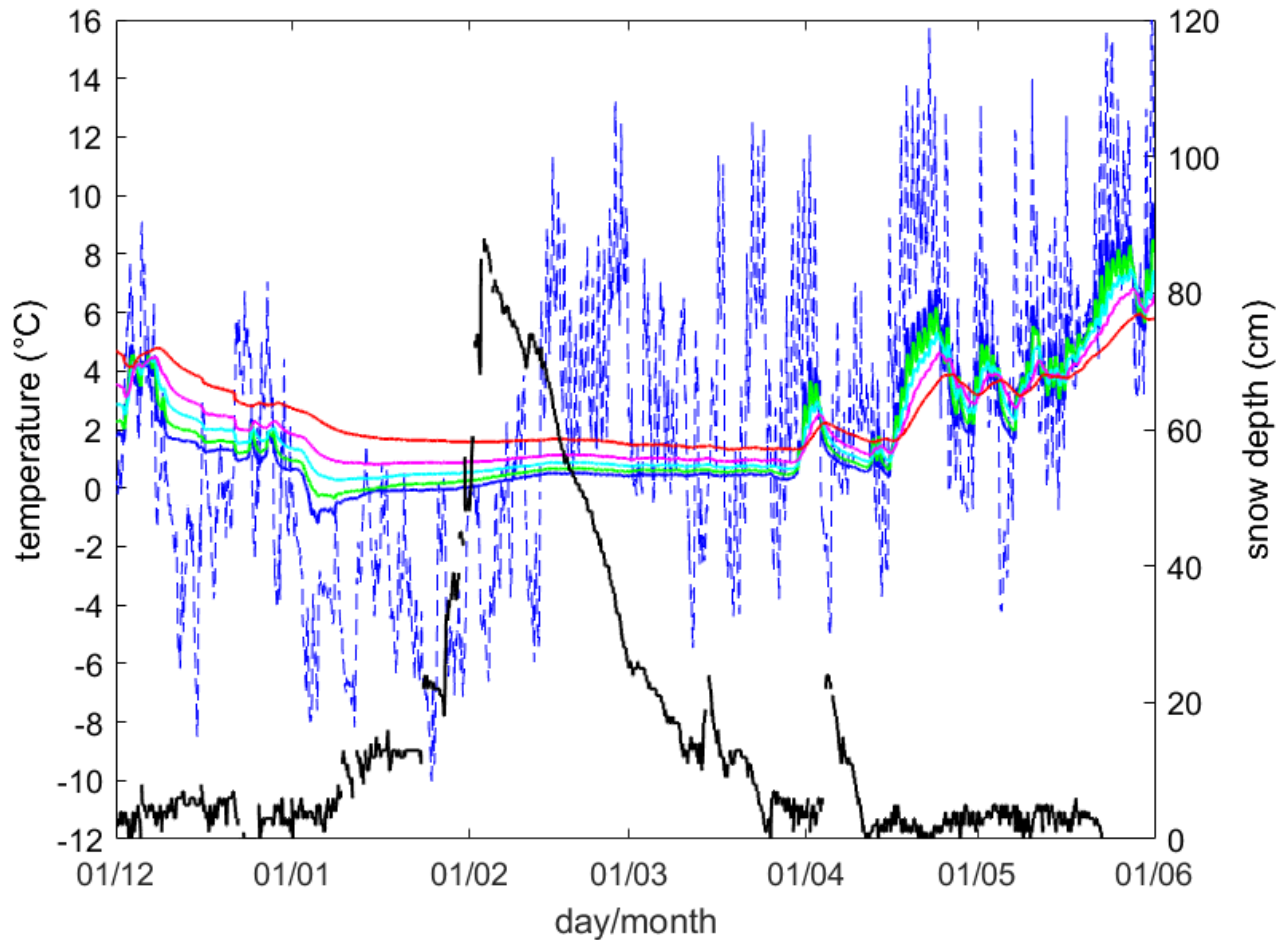
198 <sup>1</sup> height above snow-free ground

199 <sup>2</sup> spectral range in wavelength

200 <sup>3</sup> two sensors for each depth

201

202 As an example of the use of these measurements, Figure 6 shows hourly changes in air and soil temperatures and snow depth  
203 from December 2018 until June 2019, a winter characterized by deep and sustained snow cover. Snow cover began to build in  
204 late December, reaching a maximum of 90 cm in early February. Melt rates became significant as air temperatures remained  
205 consistently above 0°C through late February. Snow cover disappeared by the end of March, although there were a few  
206 snowfalls through May. Snow cover strongly affected soil temperatures to a depth of 60 cm. The disappearance of the main  
207 snow cover at the end of March suddenly reversed the temperature gradient in the soil (the deeper soil became colder than the  
208 surface). Soil temperatures were also affected by a few snowfalls in April, associated with short periods of cold weather.  
209



210  
211 Figure 6: Left axis: air temperature (blue dotted line) and soil temperature at 2.5, 8, 15, 30 and 60 cm depth (blue, green,  
212 cyan, magenta and red solid lines, respectively). Right axis: snow depth (black line). Hourly data from the weather station in  
213 the forest (Table 2) from 1 September 2018 to 1 June 2019. The data gaps in the snow depth time series are mainly due to  
214 snowfall events that disrupted the measurements.

### 215 3.3 Snow measurements

216 In order to document the spatial variability of snow cover in the forest, a transect of 18 snow poles was deployed in early  
217 winter 2016-2017 (Figure 1). The locations of these snow poles (spaced 2 m apart) were georeferenced in Lambert 93  
218 coordinates. For each pole, the snow depth was measured approximately every two weeks during the two field campaigns.  
219 Snow water equivalent measurements were carried out every week for only four poles at a time, alternating among the 18 poles  
220 to minimize destruction of the local snowpack structure. Detailed studies by Morin et al. (2012) and Lejeune et al. (2019)  
221 estimated the uncertainties in snow depth and snow water equivalent measurements to be  $\pm 1$  cm and  $\pm 5$  %, respectively, in  
222 agreement with the estimation of López-Moreno et al. (2020) derived from a comparison of measurements with different snow  
223 core samplers. Simultaneously, measurements of snow depth and water equivalent were made in the reference meadow site as  
224 described in Lejeune et al. (2019).

### 225 3.4 Precipitation tanks

226 The amount of snow held in the canopy can be large and remains difficult to measure. Due to the sublimation of intercepted  
227 snow, a large portion of the snow retained in the canopy never reaches the ground, and the interplay of interception, sublimation  
228 and delayed deposition on the ground creates significant below-forest heterogeneity in snow accumulation (e.g., Helbig et al.,  
229 2020). To try to measure snow interception by the canopy, 24 “precipitation tanks” (1 m x 0.39 m) were built and then deployed  
230 under the canopy in three eight-meter transects at the start of winter 2017-2018 (Figures 1 and 7). Snow was taken from the  
231 precipitation tanks and weighed after each of the seven significant snowfall events between 20 February and 3 April 3 2018.  
232 The uncertainties in this new measurement method developed by CEN-MeteoFrance are difficult to estimate. Vincent (2018)  
233 estimated the measurement uncertainty at about 5%, but additional studies are needed.



235

236

Figure 7: Precipitation tanks installed below the canopy (photograph by Y. Lejeune).

237

### 3.5 Rugged Laser Scan

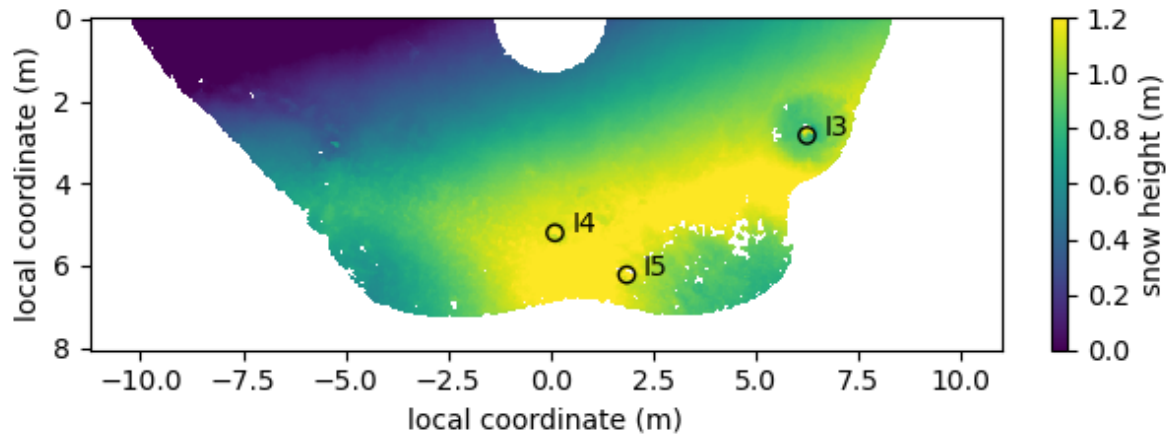
238

The Rugged Laser Scan (RLS) is a scanning laser meter that was installed at about 4 m above the ground close to the center of the main clearing to monitor spatio-temporal variations of snow depth under various canopy covers on a daily or two-daily basis (Figure 1). The device is described in detail in Picard et al. (2016) and is specially designed to monitor snow heights. It comprises a laser meter mounted on a 2-axis stage and can scan  $\approx 200000$  points in 4 hours. The laser meter was used in scan mode. With a setup at 4 m height, and azimuth angles varying from  $-90^\circ$  to  $+90^\circ$  (azimuth angle  $0^\circ$  points towards  $225^\circ$  (south-west)) and zenith angles varying from  $19^\circ$  and  $62^\circ$ , the scanned area is a half-disk of radius  $\sim 7$  m, with a surface area of about  $80 \text{ m}^2$ . The area encompasses three pairs of radiometers installed on the snow surface. Data acquired by the laser meter for a given day are processed to build a cloud of x, y, z points, which is then interpolated and averaged on a regular 3 cm grid. The grid is common to all measurement days so it is easy to compare the evolution of the snow surface. The vertical precision was evaluated to be about 3 mm and the accuracy to be 1 cm (Picard et al. 2016).

248

The RLS was operated during the two field experiments. The first season was from 22 February 2017 to 4 April 2017 (42 days) and had 42 valid acquisitions (once a day). The second season was from 5 December 2017 to 11 March 2018 (160 days) and had 81 valid acquisitions because scans were scheduled every other day during the winter (accumulation period) and every day during the melt season. Figure 8 shows an example of snow depths on 15 April 2018 and Figure 9 shows the changes in daily spatial averages of the snow depth during the 2017-18 field campaign.

253



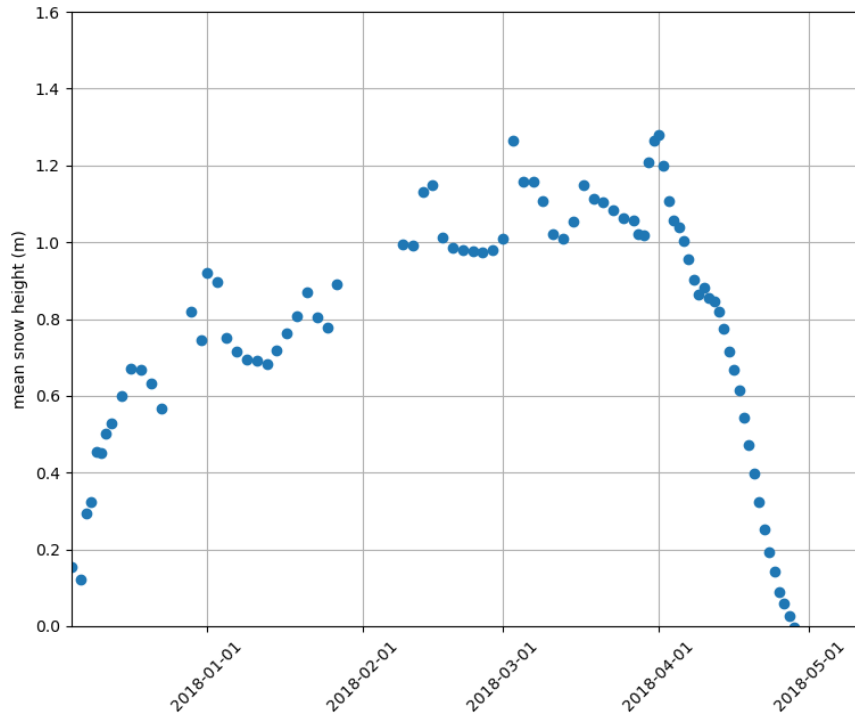
254

255

Figure 8: Snow height (m) derived from the digital terrain models (DTM) measured by the rugged Laserscan, obtained by subtracting the snow-free DTM from the 15 April 2018 DTM. The measurement area encompassed three radiometers (I3, I4 and I5).

256

257



258

259

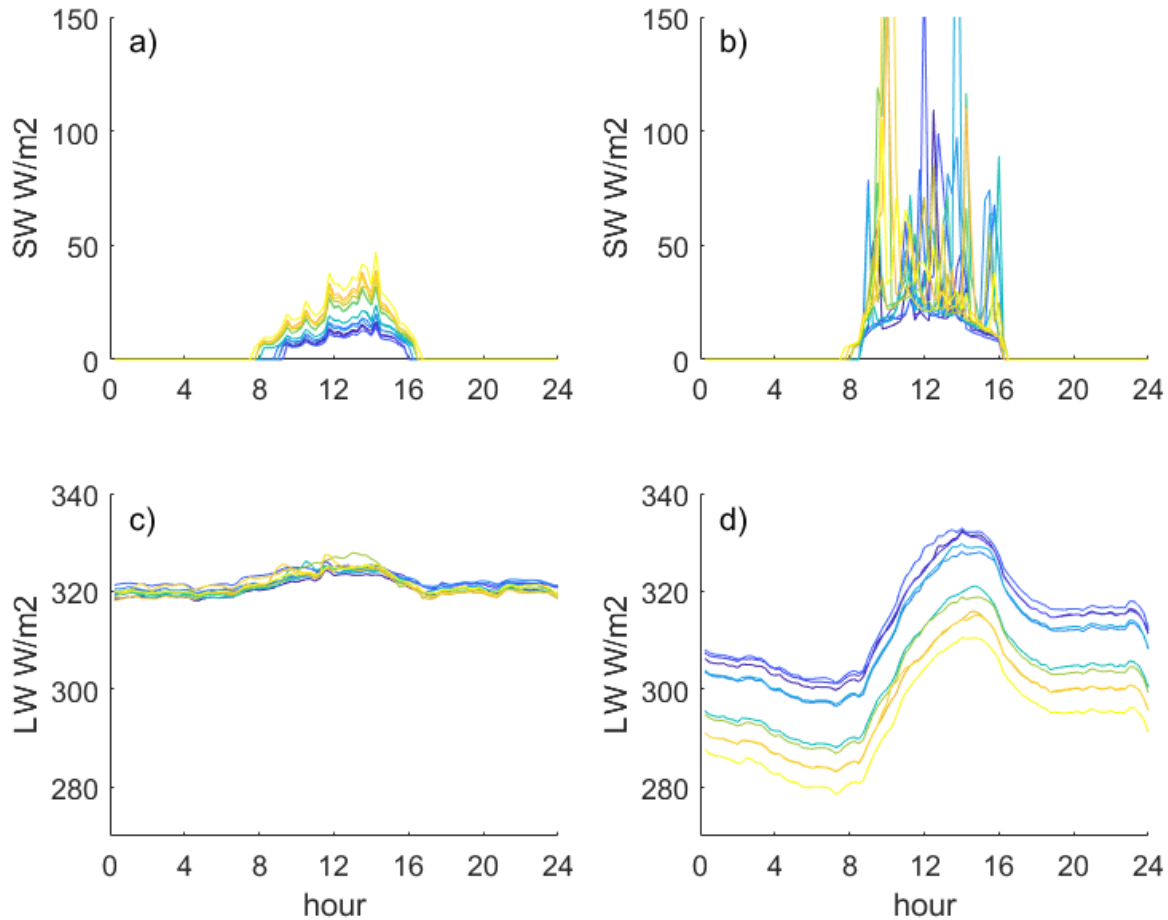
Figure 9: Daily spatial averages of the snow depth measured by the rugged Laserscan during the 2017-18 field campaign.

#### 260 4 Spatial variability, measurement uncertainties and data validation

261 This section provides estimations of the dataset uncertainties related to measurement uncertainties and spatial variability of  
 262 the variables within the measurement plot. The uncertainties of the sensors and the measurement methods have been described  
 263 in the previous sections. For meteorological measurements, sensor manufacturers generally provide reliable information on  
 264 sensor accuracy (Table 2). In this Section, comparisons of radiation, air temperature, and snow measurements at different  
 265 locations provide a better insight into the measurement uncertainties and a first validation of the data set.

266 Figure 10 illustrates the spatial variability of the incoming shortwave and longwave radiation fluxes below various forest  
 267 covers. It shows the effects of clouds and canopy cover on the sub-canopy 15-minute radiation fluxes during an overcast day  
 268 and a clear sky day of the 2017 campaign. Under thick cloud cover (January 31), shortwave radiation, mostly diffuse, reaching  
 269 the ground remains small but steadily increases with decreasing canopy cover (increasing sky view factor). Sky and vegetation  
 270 were characterized by similar temperatures and longwave emittance (close to 1), and all the pyrgeometers recorded similar  
 271 longwave radiations fluxes (within a few  $W m^{-2}$ , confirming the good accuracy of the sensors), without relation to the canopy  
 272 cover. In clear sky conditions (February 18), shortwave irradiance is mostly direct. Sunflecks on the ground below the canopy

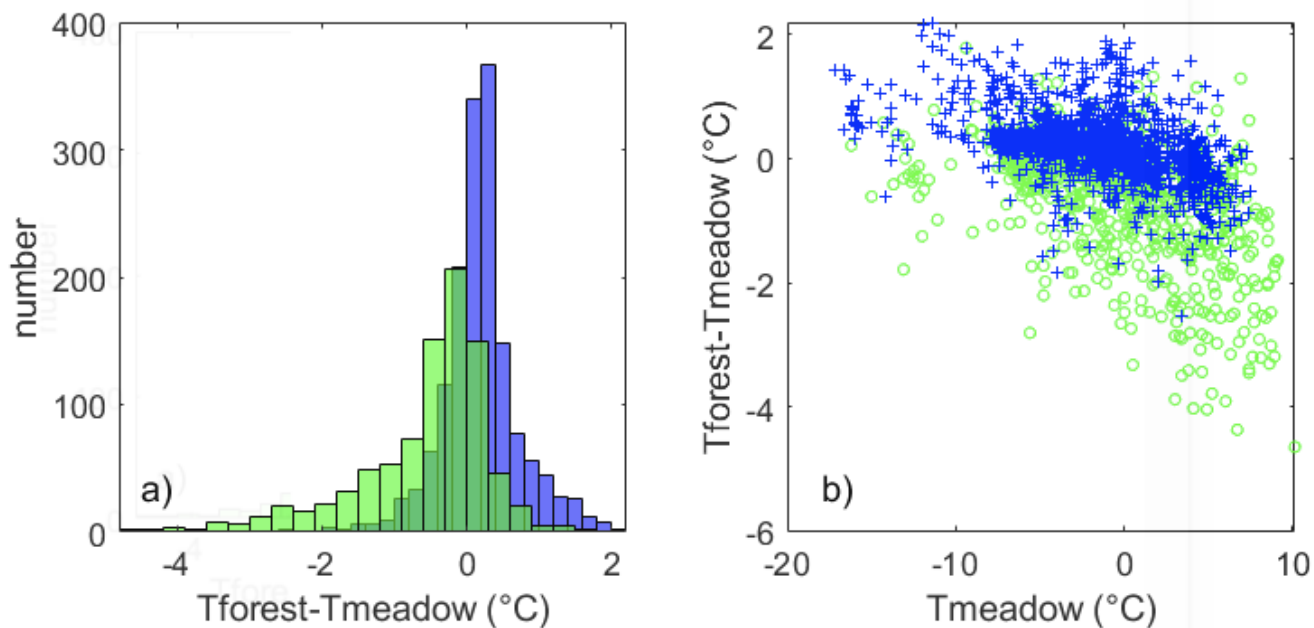
273 caused peaks of shortwave irradiance of various amplitudes and at different times at the different pyranometers, superimposed  
 274 on the diffuse shortwave radiation that has penetrated through the canopy. The diurnal changes of sub-canopy longwave  
 275 irradiance are remarkably parallel between the different measurement sites. The constant offset between the signals is related  
 276 to the canopy cover due to the large contrast between the large emittance of vegetation and the small emittance of clear, cold  
 277 sky; the larger the sky view factor, the smaller the longwave irradiance (Figure 10d).  
 278



279  
 280 Figure 10: Shortwave (a, b) and longwave (c, d) incoming radiation fluxes measured by each radiometer during an overcast  
 281 day (January 31: a, c) and during a clear-sky day (February 18: b, d). 15-minute averages of the sub-canopy fluxes during the  
 282 2017 campaign. Line color is related to the sky view factor  $V_f$  from dark blue (lowest  $V_f = 0.17$ ) to yellow (highest  $V_f = 0.32$ ).  
 283

284 Figure 11 illustrates the hourly air temperature differences between forest and meadow. During daytime, the forest is generally  
 285 a few degrees colder than the open meadow site, with the difference increasing on clear sky days when the air is warmest (high

286  $T_{open}$ ). During the night, the forest is generally slightly warmer than the meadow, with the difference reaching a few degrees  
 287 on cold clear-sky nights (low  $T_{open}$ ). Thus, average daily air temperatures are quite similar in the forest and meadow site ( $dT \sim$   
 288  $0.2^\circ\text{C}$  on average during the 2018 campaign) because warmer nights counterbalance cooler days in the forest relative to the  
 289 meadow. In addition, warmer cloudy periods tend to counterbalance cooler clear-sky periods in the forest relative to the  
 290 meadow.  
 291



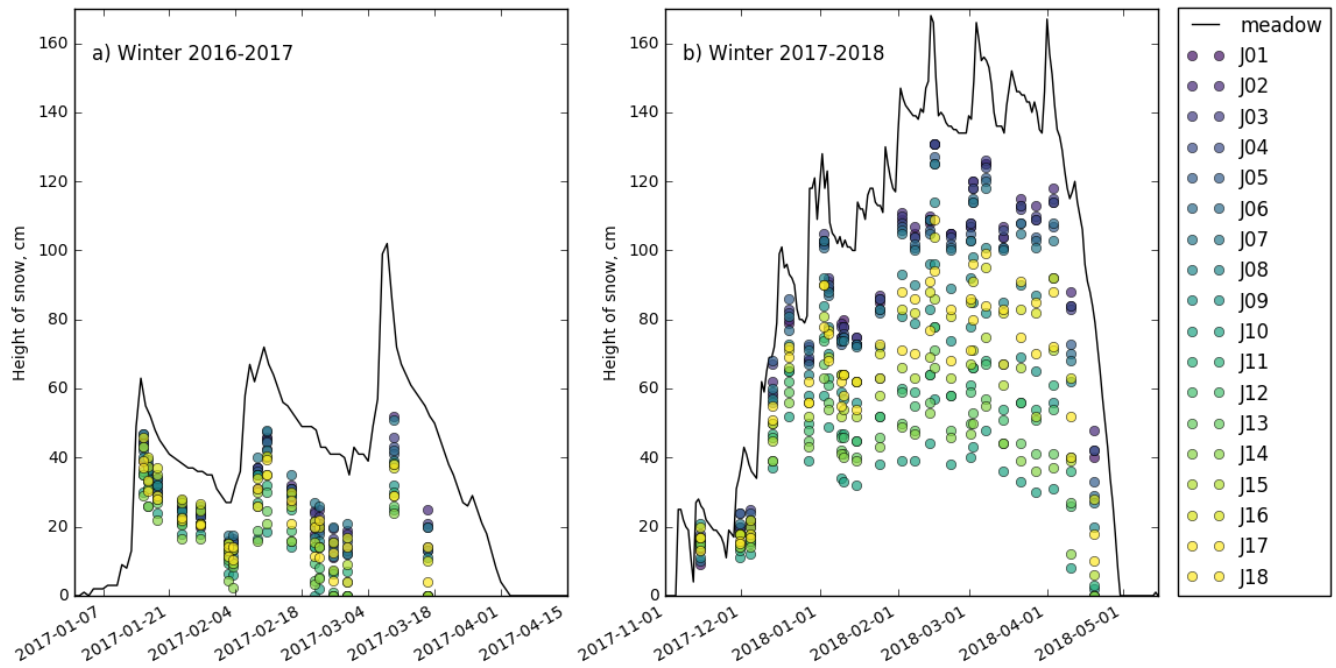
292  
 293  
 294 Figure 11: Difference of hourly air temperature between forest and meadow ( $T_{forest} - T_{meadow}$ ) during the 2018 campaign. (a)  
 295 shows histograms, (b) shows ( $T_{forest} - T_{meadow}$ ) according to  $T_{meadow}$ . The distinction between daytime (green bars and circles)  
 296 and nighttime (blue bars and crosses) values is based on a threshold on the shortwave incoming radiation fluxes in the  
 297 meadow site ( $SW < 10 \text{ W m}^{-2}$  during nighttime).  
 298

299 Figures 12 and 13 illustrate the spatial variability of snow depth and snow water equivalent measurements in the open meadow  
 300 and along the snow pole transect in the forest (see locations in Figure 1) during the 2017 and 2018 field campaigns. As  
 301 previously mentioned, snow cover lasted several weeks longer and was deeper in the second campaign than in the first, reaching  
 302 a maximum in the meadow of 160 cm and 100 cm, respectively. The seasonal maximum snow depth under the canopy was  
 303 smaller than that of the meadow by factors ranging from 0.20 to 0.75, depending on the local canopy cover. For the snow water  
 304 equivalent, these ratios ranged from 0.16 to 0.60. Relative decreases in snow depth and water equivalent in the forest transect  
 305 compared to the meadow were greater during the first campaign characterized by shallow snow cover. Figures 12 and 13



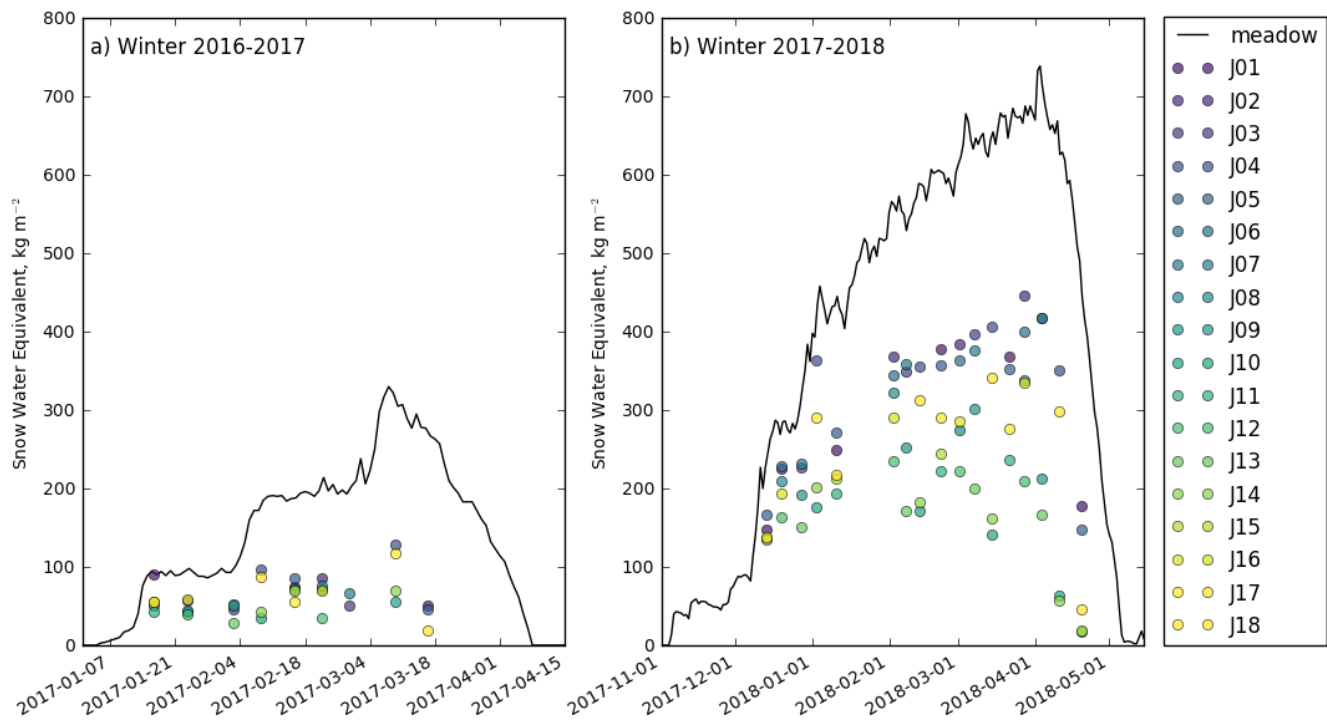
306 suggest that the effects of the forest on snow cover are more marked during the winter accumulation season (likely due to  
 307 interception of snow by the canopy), whereas melt rates during the short ablation season appear to be quite similar in the forest  
 308 and the meadow. Snow generally disappears earlier in the forest than in the open meadow, but differences in the duration of  
 309 snow cover are generally small, except in years of low snowfall, and highly location-dependent due to the high spatial  
 310 variability of snow depth in the forest (Figures 12 and 13). This is in line with the meta-analysis of Lundquist et al. (2013) for  
 311 a dense forest site in a mild climate, but further analysis of snow and meteorological data is needed to investigate this issue at  
 312 Col de Porte.

313  
 314



315  
 316 Figure 12: Reference snow depth measured in the meadow from Lejeune et al., 2019 (black line) and manually measured at  
 317 the snow pole transect in the forest (circles, each color corresponds to a snow pole, Figure 1) during the 2017 (a) and 2018  
 318 (b) field campaigns.

319



320

321 Figure 13: Reference Snow Water Equivalent measured in the meadow site with a cosmic ray neutron sensor (black line, see  
 322 details in Lejeune et al., 2019) and manually measured at the snow pole transect in the forest (circles, each color corresponds  
 323 to a snow pole, [Figure 1](#)) during the 2017 (a) and 2018 (b) field campaigns.

324

## 325 **5 Conclusions**

326 The datasets collected in the Col de Porte coniferous forest will allow research on the effects of the canopy on snow  
 327 accumulation and ablation processes under different canopy covers. Two intensive field campaigns were conducted during the  
 328 winters of 2016-17 and 2017-18 and an automatic weather station has been maintained under the canopy since then.  
 329 Meteorological and snow measurements (automatic weather station, radiometer array, snow pole transect, laser scan,  
 330 precipitation tanks to estimate snow interception by the canopy) were complemented by canopy observations (tree inventory,  
 331 LIDAR measurements of forest structure, sub-canopy hemispherical photographs). Continuous measurements throughout the  
 332 year at high temporal frequency (15-minute) from the meteorological station allow hydrological and ecological studies related  
 333 to seasonal changes in micrometeorological and soil conditions.

334 **Data availability**

335 All datasets described and presented in this paper can be openly accessed from the repository of the Observatoire des Sciences  
336 de l'Univers de Grenoble (OSUG) data center at: <http://dx.doi.org/10.17178/SNOUF.2022> (Sicart et al., 2022). Table 3  
337 provides the links to the different datasets.

338

339 Table 3: Links to the dataset repository.

Data set	Period	Format	Repository
Forest inventory	13-14 September 2016 27 July 2018	csv	<a href="https://doi.osug.fr/data/public/SNOUF/forest/">https://doi.osug.fr/data/public/SNOUF/forest/</a>
Hemispherical photographs	4 September 2017	png	<a href="https://doi.osug.fr/data/public/SNOUF/hemispherical-photos/">https://doi.osug.fr/data/public/SNOUF/hemispherical-photos/</a>
Rugged laser scan	22 Feb to 4 April 2017 5 Dec 2017 to 13 May 2018	netCDF	<a href="https://doi.osug.fr/data/public/SNOUF/laser-scan/">https://doi.osug.fr/data/public/SNOUF/laser-scan/</a>
Airborne laser scanning	30 August and 2 September 2016	laz	<a href="https://doi.osug.fr/data/public/SNOUF/lidar/">https://doi.osug.fr/data/public/SNOUF/lidar/</a>
Weather station and radiometer array measurements	16 Jan 2016 to 14 June 2022	csv	<a href="https://doi.osug.fr/data/public/SNOUF/meteorological/">https://doi.osug.fr/data/public/SNOUF/meteorological/</a>
Snow pole and precipitation tank measurements	16 Jan 2016 to 21 March 2017 1 Dec 2017 to 15 March 2018	xlsx	<a href="https://doi.osug.fr/data/public/SNOUF/snow/">https://doi.osug.fr/data/public/SNOUF/snow/</a>

340

341 **Author contributions**

342 JES organized the data and wrote the first draft of the manuscript. JMM and YL cleaned and corrected the forest and snow  
343 measurements, respectively. LA and GP cleaned and corrected the laser scan measurements. VR and DS analyzed the  
344 meteorological data. All authors participated in the field campaigns, collected and assembled data records, and contributed to  
345 writing the paper.

346 **Competing interests**

347 The authors declare that they have no conflict of interest.

348 **Disclaimer**

349 Any reference to specific equipment types or manufacturers is for informational purposes and does not represent a product  
350 endorsement.

351 **Acknowledgments and funding**

352 This project was conducted within the grant Labex OSUG@2020 ANR10 LABX56 UGA and with financial support from the  
353 IGE and the CEN, through a collaboration between the French institutes IGE, CEN and INRAE, and the universities of  
354 Edinburgh and Northumbria in the UK. Marie Dumont has received funding from the European Research Council (ERC) under  
355 the European Union's Horizon 2020 research and innovation program (IVORI; grant no. 949516). We thank Laurent Bourges  
356 (CNRS, OSUG) for his support in managing the dataset.

357 **References**

- 358 Boone, A., Samuelsson, P., Gollvik, S., Napoly, A., Jarlan, L., Brun, E., and Decharme, B.: The interactions between soil-  
359 biosphere-atmosphere land surface model with a multi-energy balance (ISBA-MEB) option in SURFEXv8-Part 1: Model  
360 description, *Geosci. Model Dev.*, 10, 843-872, 10.5194/gmd-10-843-2017, 2017.
- 361 Durot, K., Modélisation hydrologique distribuée du bassin versant nivo-pluvial de Sarennes. Validation des données d'entrées  
362 et **développement** d'un module de fonte nivale sous forêt, PhD. thesis, Laboratoire d'Etude des Transferts en Hydrologie et  
363 Environnement, UJF, 332 pp., 1999.
- 364 Ellis, C. R., Pomeroy, J. W., and Link, T. E.: Modeling increases in snowmelt yield and desynchronization resulting from forest  
365 gap-thinning treatments in a northern mountain headwater basin, *Water Resources Research*, 49, 936-949,  
366 10.1002/wrcr.20089, 2013.
- 367 Elzinga, C., Shearer, R. C., and Elzinga, G.: Observer Variation in Tree Diameter Measurements, *Western Journal of Applied*  
368 *Forestry*, 20, 134-137, 10.1093/wjaf/20.2.134, 2005.
- 369 Essery, R.: Large-scale simulations of snow albedo masking by forests, *Geophysical Research Letters*, 40, 5521-5525, 2013.
- 370 Essery, R., Bunting, P., Rowlands, A., Rutter, N., Hardy, J., Melloh, R., Link, T., Marks, D., and Pomeroy, J.: Radiative transfer  
371 modeling of a coniferous canopy characterized by airborne remote sensing, *J. Hydrometeorol.*, 9, 228-241, 2008.
- 372 Essery, R., Rutter, N., Pomeroy, J., Baxter, R., Stahli, M., Gustafsson, D., Barr, A., Bartlett, P., and Elder, K.: An Evaluation of  
373 Forest Snow Process Simulations, *Bull. Amer. Meteorol. Soc.*, 90, 1120-1136, 10.1175/2009bams2629.1, 2009.
- 374 Gouttevin, I., Lehning, M., Jonas, T., Gustafsson, D., and Molder, M.: A two-layer canopy model with thermal inertia for an  
375 improved snowpack energy balance below needleleaf forest (model SNOWPACK, version 3.2.1, revision 741), *Geosci. Model*  
376 *Dev.*, 8, 2379-2398, 10.5194/gmd-8-2379-2015, 2015.
- 377 Halldin, S., and A. Lindroth: Errors in Net Radiometry: Comparison and Evaluation of Six Radiometer Designs, *Journal of*  
378 *Atmospheric and Oceanic Technology*, 9(6), 762-783, 1992.
- 379 Helbig, N., Moeser, D., Teich, M., Vincent, L., Lejeune, Y., Sicart, J. E., and Monnet, J. M.: Snow processes in mountain forests:  
380 interception modeling for coarse-scale applications, *Hydrology and Earth System Sciences*, 24, 2545-2560, 10.5194/hess-24-  
381 2545-2020, 2020.

382 Hojatimalekshah, A., Uhlmann, Z., Glenn, N. F., Hiemstra, C. A., Tennant, C. J., Graham, J. D., Spaete, L., Gelvin, A., Marshall,  
383 H. P., McNamara, J. P., and Enterkine, J.: Tree canopy and snow depth relationships at fine scales with terrestrial laser  
384 scanning, *The Cryosphere*, 15, 2187-2209, 10.5194/tc-15-2187-2021, 2021.

385 Jonas, T., Webster, C., Mazzotti, G., and Malle, J.: HPEval: A canopy shortwave radiation transmission model using high-  
386 resolution hemispherical images, *Agric. For. Meteorol.*, 284, 9, 10.1016/j.agrformet.2020.107903, 2020.

387 Lejeune, Y., Dumont, M., Panel, J.-M., Lafaysse, M., Lapalus, P., Le, E., Gac, B. L., and Morin, S.: 57 years (1960-2017) of  
388 snow and meteorological observations from a mid-altitude mountain site (Col de Porte, France, 1325 m alt.), *Earth System  
389 Science Data Discussions*, 2018, 1-25, 2019.

390 López-Moreno, J. I., Leppänen, L., Luks, B., Holko, L., Picard, G., Sanmiguel-Valladolid, A., Alonso-González, E., Finger, D.  
391 C., Arslan, A. N., and Gillemot, K.: Intercomparison of measurements of bulk snow density and water equivalent of snow  
392 cover with snow core samplers: Instrumental bias and variability induced by observers, *Hydrological Processes*, 34, 3120-  
393 3133, 2020.

394 Lundquist, J. D., Dickerson-Lange, S. E., Lutz, J. A., & Cristea, N. C.: Lower forest density enhances snow retention in regions  
395 with warmer winters: A global framework developed from plot-scale observations and modeling. *Water Resources Research*,  
396 49(10), 6356-6370, 2013.

397 Luoma, V., Saarinen, N., Wulder, M. A., White, J. C., Vastaranta, M., Holopainen, M., and Hyyppä, J.: Assessing Precision in  
398 Conventional Field Measurements of Individual Tree Attributes, *Forests*, 8, 38, 2017.

399 Malle, J., Rutter, N., Mazzotti, G., and Jonas, T.: Shading by Trees and Fractional Snow Cover Control the Subcanopy Radiation  
400 Budget, *Journal of Geophysical Research: Atmospheres*, 124, 3195-3207, 10.1029/2018jd029908, 2019.

401 Mazzotti, G., Essery, R., Moeser, C. D., and Jonas, T.: Resolving Small-Scale Forest Snow Patterns Using an Energy Balance  
402 Snow Model With a One-Layer Canopy, *Water Resources Research*, 56, e2019WR026129,  
403 <https://doi.org/10.1029/2019WR026129>, 2020.

404 Mazzotti, G., Currier, W. R., Deems, J. S., Pflug, J. M., Lundquist, J. D., and Jonas, T.: Revisiting Snow Cover Variability and  
405 Canopy Structure Within Forest Stands: Insights From Airborne Lidar Data, *Water Resources Research*, 55, 6198-6216,  
406 10.1029/2019wr024898, 2019.

407 Michel, D., et al.: Performance and uncertainty of CNR1 net radiometers during a one-year field comparison, *Journal of  
408 Atmospheric and Oceanic Technology*, 25(3), 442-451, 2008.

409 Morin, S., Lejeune, Y., Lesaffre, B., Panel, J. M., Poncet, D., David, P., and Sudul, M.: An 18-yr long (1993-2011) snow and  
410 meteorological dataset from a mid-altitude mountain site (Col de Porte, France, 1325m alt.) for driving and evaluating  
411 snowpack models, *Earth Syst. Sci. Data*, 4, 13-21, 10.5194/essd-4-13-2012, 2012.

412 Musselman, K. N., Molotch, N. P., Margulis, S. A., Lehning, M., and Gustafsson, D.: Improved snowmelt simulations with a  
413 canopy model forced with photo-derived direct beam canopy transmissivity, *Water Resources Research*, 48, 2012.

414 Nobis, M., and U. Hunziker: Automatic thresholding for hemispherical canopy-photographs based on edge detection,  
415 *Agricultural and Forest Meteorology*, 128(3-4), 243-250, 10.1016/j.agrformet.2004.10.002, 2005.

416 Otterman, J., Staenz, K., Itten, K. I., and Kukla, G.: Dependence of Snow Melting and Surface-Atmosphere Interactions on the  
417 Forest Structure, *Bound.-Layer Meteor.*, 45, 1-8, 10.1007/bf00120812, 1988.

418 Philipona, R., et al.: Atmospheric longwave irradiance uncertainty: Pyrgeometers compared to an absolute sky-scanning  
419 radiometer, atmospheric emitted radiance interferometer, and radiative transfer model calculations, *Journal of Geophysical*  
420 *Research-Atmospheres*, 106(D22), 28129-28141, 2001.

421 Picard, G., Arnaud, L., Panel, J. M., and Morin, S.: Design of a scanning laser meter for monitoring the spatio-temporal evolution  
422 of snow depth and its application in the Alps and in Antarctica, *The Cryosphere*, 10, 1495-1511, 2016.

423 Pomeroy, J., Rowlands, A., Hardy, J., Link, T., Marks, D., Essery, R., Sicart, J. E., and Ellis, C.: Spatial Variability of Shortwave  
424 Irradiance for Snowmelt in Forests, *J. Hydrometeorol.*, 9, 1482-1490, 10.1175/2008jhm867.1, 2008.

425 Reid, T., Essery, R., Rutter, N., and King, M.: Data-driven modelling of shortwave radiation transfer to snow through boreal  
426 birch and conifer canopies, *Hydrological Processes*, 28, 2987-3007, 2014.

427 Röhle, H.: Vergleichende Untersuchungen zur Ermittlung der Genauigkeit bei der Ablotung von Kronenradien mit dem Dachlot  
428 und durch senkrecht Anvisieren des Kronenrandes (Hochblick-Methode), *Forstarchiv*, 57 (1), pp. 67-71, 1986.

429 Rutter, N., Essery, R., Pomeroy, J., Altimir, N., Andreadis, K., Baker, I., Barr, A., Bartlett, P., Boone, A., Deng, H. P., Douville,  
430 H., Dutra, E., Elder, K., Ellis, C., Feng, X., Gelfan, A., Goodbody, A., Gusev, Y., Gustafsson, D., Hellstrom, R., Hirabayashi,  
431 Y., Hirota, T., Jonas, T., Koren, V., Kuragina, A., Lettenmaier, D., Li, W. P., Luce, C., Martin, E., Nasonova, O., Pumpanen,  
432 J., Pyles, R. D., Samuelsson, P., Sandells, M., Schadler, G., Shmakina, A., Smirnova, T. G., Stahli, M., Stockli, R., Strasser, U.,  
433 Su, H., Suzuki, K., Takata, K., Tanaka, K., Thompson, E., Vesala, T., Viterbo, P., Wiltshire, A., Xia, K., Xue, Y. K., and  
434 Yamazaki, T.: Evaluation of forest snow processes models (SnowMIP2), *J. Geophys. Res.-Atmos.*, 114, 18, D06111,  
435 10.1029/2008jd011063, 2009.

436 Sicart et al.: Snow Under Forest. Snow, forest and meteorological measurements at Col de Porte, SNOUF-OSUG [data set],  
437 <http://dx.doi.org/10.17178/SNOUF.2022>, 2022.

438 Van den Broeke, M., et al.: Surface radiation balance in Antarctica as measured with automatic weather stations, *Journal of*  
439 *Geophysical Research*, 109(D09103), doi:10.1029/2003JD004394, 2004.

440 Vincent, L.: Observation et modélisation du manteau neigeux sous une forêt d'épicéas au Col de Porte, Thèse de Master 2,  
441 Université Paul Sabatier, Toulouse, 40 pp., 2018.

442 Vionnet, V., Brun, E., Morin, S., Boone, A., Faroux, S., Le Moigne, P., Martin, E., and Willemet, J. M.: The detailed snowpack  
443 scheme Crocus and its implementation in SURFEX v7. 2, *Geosci. Model Dev.*, 5, 773-791, 2012.

444 Webster, C., Rutter, N., Zahner, F., and Jonas, T.: Modeling subcanopy incoming longwave radiation to seasonal snow using air  
445 and tree trunk temperatures, *Journal of Geophysical Research: Atmospheres*, 121, 1220-1235, 2016.